RESEARCH ARTICLE

ADVANCED
PHOTONICS
RESEARCH
Open Access

www.adpr-journal.com

Far-Field Synthetic Aperture Imaging via Fourier Ptychography with Quasi-Plane Wave Illumination

*Sheng Li, Bowen Wang, Kunyao Liang, Qian Chen, and Chao Zuo**

Fourier ptychography (FP) technique is a promising super-resolution tool in noninterferometric synthetic aperture research thanks to its unique capabilities for circumventing the physical limitation of space bandwidth product. However, FP imaging in the long-range scenario suffers from field-of-view (FOV) attenuation due to spherical-wave imaging characteristics, and the speckle noise of most targets further restricts the FP's application in far-field detection. Herein, a remote FP (R-FP) technique is proposed to address the issues by combining the idea of quasi-plane wave illumination and the total variation-guided filtering (TVGF) method. Compared with conventional macroscopic Fourier ptychographic imaging, R-FP overcomes the contradiction between FOV and detection range and mitigates the effect of speckle noise by utilizing the TVGF method, as demonstrated by high-resolution imaging of various targets (including United States Air Force (USAF) resolution chart, spade poker, and fingerprint). In particular, the long-range FP capability of the proposed approach is demonstrated by the synthetic aperture imaging of a King poker card at 12 m away. To the best of the authors' knowledge, R-FP achieves the farthest detection range of macroscopic Fourier ptychographic imaging up to date, demonstrating its potential for application in far-field detection.

1. Introduction

Acquiring high-resolution images is essential in far-field imaging application such as astronomy, remote sensing, and geological exploration. Especially in astronomy, astronomers attempted to increase the finite aperture size in detection

S. Li, B. Wang, K. Liang, Q. Chen, C. Zuo
School of Electronic and Optical Engineering
Nanjing University of Science and Technology
No. 200 Xiaolingwei Street, Nanjing, Jiangsu Province 210094, China
E-mail: zuochao@njust.edu.cn

S. Li, B. Wang, K. Liang, Q. Chen, C. Zuo
Smart Computational Imaging Laboratory (SCILab)
Nanjing University of Science and Technology
Nanjing, Jiangsu Province 210094, China

S. Li, B. Wang, K. Liang, Q. Chen, C. Zuo
Jiangsu Key Laboratory of Spectral Imaging and Intelligent Sense
Nanjing, Jiangsu Province 210094, China

The ORCID identification number(s) for the author(s) of this article can be found under https://doi.org/10.1002/adpr.202300180.

systems for higher spatial resolution according to the Rayleigh criterion, yet, with that comes higher costs, complex aberrations, and tough manufacturing processes, which have hindered the development of far-field detection by larger apertures. Synthetic aperture (SA) is a remote sensing technique that combines multiple subaperture images to form a high-resolution image, exceeding the diffraction limit of a single aperture.[1,2] Over the last several decades, the SA technique, as a powerful tool for detection and imaging in a variety of complex scenarios, has been widely applied in several fields, e.g., SA radar (SAR),[3,4] inverse SA radar (ISAR),[5] and SA sonar.[6] As their antenna can record the full complex field (amplitude and phase) of microwave, most SA techniques are appropriate for radar, but when they are used for visible imaging, the phase information will be lost. In other words, the SA technique applied to visible imaging has for a long time been limited.

As a promising and elegant computational imaging approach, the Fourier ptychography (FP) technique has achieved the best of both worlds (high resolution and wide field) with the characteristics of phase recovery and the idea of SA.[7–11] It has been demonstrated for label-free imaging of biological samples without the necessity of interferometric methods to acquire phase.[12] In particular, various systems and methods have been developed for high-precision Fourier ptychographic microscopy (FPM),[13–15] e.g., Fourier ptychographic diffraction tomography for 3D microscopy,[16] high spatio-temporal resolution imaging over a long-time scale,[17] UV Fourier ptychographic microscopy[18] to achieve higher spatial resolution, and high-performance FP with deep learning.[19–21] The stability and reconstruction quality may be significantly degraded with non-negligible noise when the ptychographical iterative engine (PIE) and extended ptychographic iterative engine (ePIE) are used for phase recovery. Adaptive compensation[22] and simulated annealing correction algorithms[23] have also been proposed to tackle the artifact phenomenon in the reconstruction results, providing fast convergence speed with few computational overheads. Owing to the rise of aperture scanning techniques[24] and their flexibility for the spectrum recovery as a far-field detection scheme,[25,26] many efforts to refine the macroscopic FP framework have been made.[27–29] To satisfy the condition that the illumination source and camera are placed on the same side of the target, the reflective macroscopic FP has been applied

**ADVANCED
SCIENCE NEWS**

www.advancedsciencenews.com

**ADVANCED
PHOTONICS
RESEARCH**

www.adpr-journal.com

to various types of targets at the range of 1 m,[30] promoting the progress of macroscopic imaging techniques. Beyond the increased spatial resolution and space bandwidth product (SBP), the FP can achieve high precision and high-temporal resolution by pose correction scheme,[31] sparse apertures method,[32] and learning-based single-shot SA imaging method.[33] In addition, FP techniques with few photons[34] and single photon[35] are proposed to improve the sensitivity in detection. Nevertheless, due to the complex spherical wave propagation process involved, the field-of-view (FOV) of the imaging system gradually decreases as the imaging range increases, leaving the existing macroscopic FP imaging range without further expansion. In other words, if the imaging range is increased straightforwardly, the existing FP imaging system would lead to a rapid attenuation of the FOV and would not be able to obtain high-resolution imaging results over a wide field. On the other hand, most far-field FP failed to consider the optical coherence disturbance by the rough object,[36,37] which may directly result in speckle noise intensification and hinder the widespread adoption of FP in remote sensing.

In this work, we present a new noninterferometric SA technique, termed remote FP, which is capable of "regenerating" the lost FOV and corresponding spectrum information with the quasi-plane wave. Unlike the conventional macroscopic FP that cannot achieve the wide-field recording of the detection target at a long range, our method, with the ability to avoid the FOV attenuation, can be viewed as an advanced extension of the FP technique for macroscopic imaging. Furthermore, speckles in coherent imaging will obscure features on the order of diffraction limit size as it will not be possible to attribute intensity variations to the underlying signal or to the speckles themselves,

we propose a total variation-guided filtering (TVGF) method to mitigate the ill-posedness of speckle noise. The various high-resolution results reconstructed by the remote FP (R-FP) method are demonstrated, including the USAF resolution chart, spades poker, and the fingerprint produced on the coverslip. We further demonstrate super-resolution imaging of a king poker at 12 m away, suggesting the developed R-FP can provide an efficient wide-field and high-resolution imaging method for far-field macroscopic reflectance observations.

2. Principles and Methods

To acquire high-resolution images at long range, the proposed R-FP imaging system presents wide-field advantage over the conventional macro FP system, and the corresponding diagram of R-FP is shown in **Figure 1**. During the image acquisition process, a quasi-plane wave is formed by the lens 1 and lens 2 to illuminate the target with large FOV, and the reformulation of the corresponding spectrum is performed with a pair of lenses (paired lens 1 and paired lens 2). A detector on the same side of the laser source records the scattered information from the far-field target. We placed paired lenses in front of the aperture to achieve spectrum reformation because the conventional macroscopic FP system fails to record the spectrum information directly on the reflected quasi-plane waves. Considering reforming the spectrum in front of the aperture, the range between the paired lenses is required to be less than the sum of the focal lengths ($f_3 + f_4$) of the paired lenses. As the quadratic phase term in propagation is not eliminated by the modulation of the paired lenses, the phase term ζ_e generated by unequal
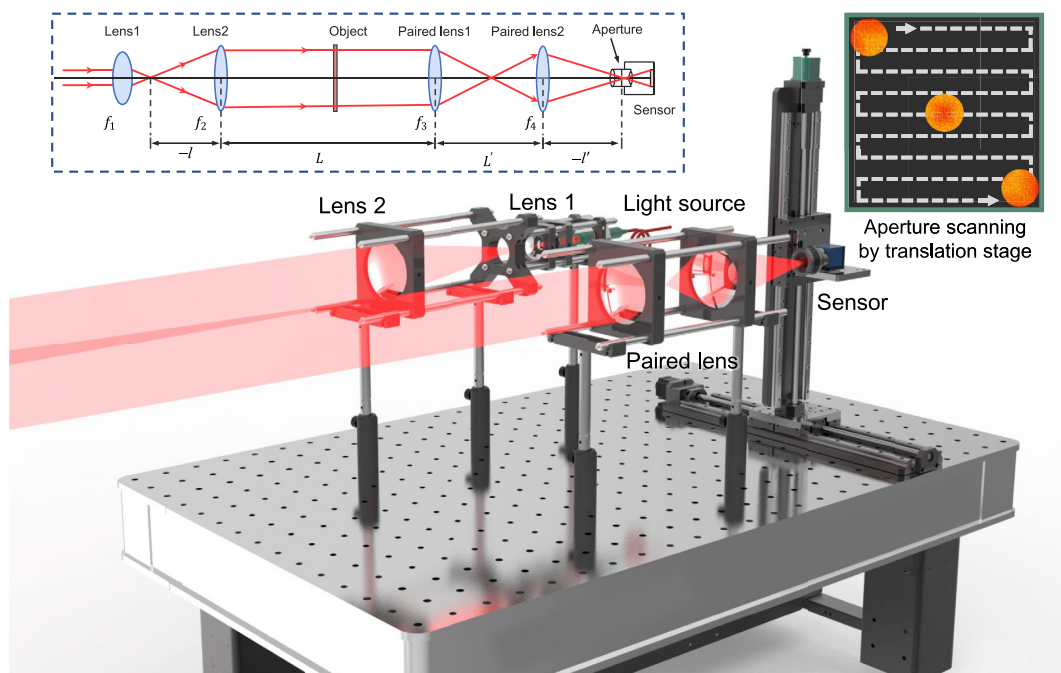

Figure 1. Overview of the proposed R-FP framework. Lens 1 and lens 2 for generation of the quasi-plane wave. The object is illuminated by a fiber laser, and the spectrum is formed behind the paired lens 2. The specific optical path tracing diagram is shown in the upper left-hand corner, and the aperture scanning with the translation stage is shown in the upper right-hand corner.

distance has to be taken into account. The optical field of the detector is expressed as

$$O_i = F^{-1}\{P(k_x, k_y)O(k_x - k_{xi}, k_y - k_{yi})\zeta_e\} \tag{1}$$

where $P(k_x, k_y)$ is the pupil function, i is the subaperture position, and F^{-1} is the inverse Fourier transform. Fortunately, the optical field information is ultimately captured by the detector in the form of intensity, which means the image is not influenced by the phase term ζ_e. The recorded intensity is demonstrated as

$$I_i = |F^{-1}\{P(k_x, k_y)O(k_x - k_{xi}, k_y - k_{yi})\}|^2 \tag{2}$$

Figure 2 summarizes the differences between conventional FP and proposed R-FP in imaging. For both approaches, an object is placed in the spatial domain, and a detector is placed in the far field for diffraction data recording. In general, the FOV of both transmissive and reflective FP systems decreases significantly as the imaging distance increases. For transmissive systems, the farther the target is from the light source, the reduced the imaging FOV. For the reflective system, as the camera and the light source are on the same side, the farther the target is from both, the imaging FOV decreases proportionally. As the object shifts away, the FOV in the conventional FP method decreases linearly until almost no image information is available. Therefore, the conventional FP approach conducts experiments within 1 m alone to avoid the FOV reduction. In contrast, the R-FP method adjusts the propagating beam to a quasi-plane wave (using a convergence angle of the quasi-plane beam to avoid power loss) for the target illumination, achieving the nonvariable FOV acquisition possible despite the increased range between the target and the detector. More precisely, to obtain the equal FOV as the R-FP method, the lens f_1 must be close to the object with the FP method, which restricts the application of reflection imaging at long range. Theoretically, the proposed R-FP method allows the extension of the detection range to an arbitrary far field with laser power enhancement.

The reconstruction result of the conventional FP approach is restricted in terms of FOV, which affects the imaging range in far-field detection. In addition, diffuse complex targets containing rough surfaces may affect the signal-to-noise ratio of the high-resolution reconstruction results. For most common targets, the diffuse reflective nature of rough surfaces evokes speckle noise, resulting in degraded image quality. With the evolution of image-denoising technology, numerous denoising methods mitigate the speckle noise of rough objects,[38,39] though the corresponding application, in reality, is not yet available as far as we know. As a more general technique for inverse problems, TV regularization methods have demonstrated promising performance in the denoising field, by addressing optimization problems to estimate complex amplitude distributions with less speckle noise.[40] We attenuate the effect of speckle noise on the reconstructed images by incorporating TV regularization into the reconstructed process. However, the key problem is mainly to separate the stripe noise and high-frequency components, which is difficult due to the mixing and overlapping between them. In particular, for speckle noise images, the noise will be more prominent than the texture information at the edges of the image.[41]
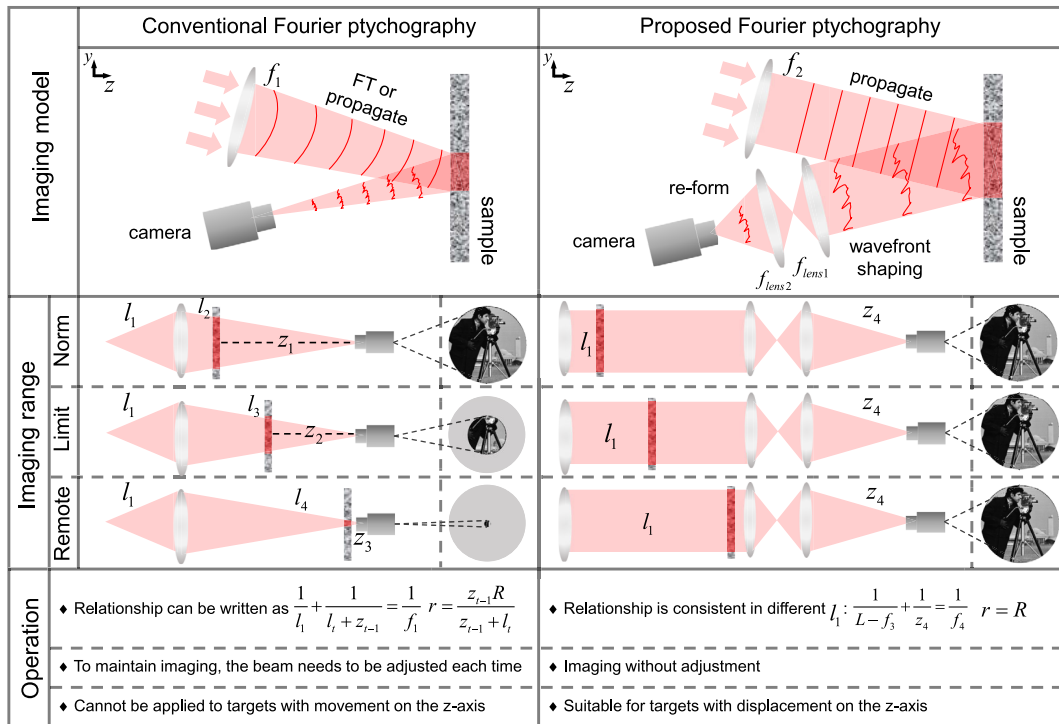

Figure 2. Comparison between conventional FP and proposed R-FP. Conventional FP technique requires the inclusion of a focusing lens to satisfy the far-field imaging conditions and acquire images in the spectrum plane. The detection target is behind the focusing lens, resulting in a sharp reduction in the FOV when the detection range is increased. R-FP technique utilizes quasi-plane waves to avid the FOV attenuation.

**ADVANCED
SCIENCE NEWS**

www.advancedsciencenews.com

**ADVANCED
PHOTONICS
RESEARCH**

www.adpr-journal.com

We further mitigate the effect of speckle noise by incorporating the guided filter in the reconstruction process. The result of each iteration is utilized as a guided image to obtain the final output image with enhanced texture information, achieving high signal-to-noise ratio SA imaging.

The flow chart of the reconstruction of the target utilizing TVGF method in R-FP is shown in **Figure 3**, the spectrum is sampled by a binary mask (corresponding to the pupil function in FP), and the TV regularization solves the spectrum estimation in a linear operator form

$$\min_x \tau\|G_x\|_1 + \frac{1}{2}\sum_{i=1}^{N} \||F^{-1}(P \cdot K_i Fx)| - b_i\|_2^2 \qquad (3)$$

where $\|G_x\|_1$ represents the anisotropic version of the TV regularization term and G denotes the gradient operator. K_i is the shifting operator; b_i is the amplitude of the measurement. Fx is the subaperture complex amplitude. The augmented Lagrangian function of the problem is given by

$$\begin{aligned} L_{RTV}(\psi,\omega,j_i,\gamma_i,w) = & \quad \tau\|\omega\|_1 + \frac{1}{2}\sum_{i=1}^{N}\||j_i| - b_i\|_2^2 \\ & + \frac{\mu}{2}\sum_{i=1}^{N}\|Fj_i - P \cdot K_i\psi + \frac{1}{\mu}\gamma_i\|_2^2 \\ & + \frac{\eta}{2}\sum_{i=1}^{N}\|\omega - GF^{-1}\psi + \frac{1}{\eta}w\|_2^2 \end{aligned} \qquad (4)$$

where γ and w are the Lagrangian multipliers, and μ, η are the penalty parameters. j_i is the complex amplitude to be updated. In contrast to conventional FP, the TV regularization-based update utilizes the alternating direction method (ADM) to achieve a complete reconstruction of the spectrum. During the iteration, the variables are updated sequentially. The update process is represented as

$$j_i = \frac{b_i + \mu|K_i|}{1 + \mu}\text{sgn}(k_i), K_i = F^{-1}(P \cdot K_i\psi) - \gamma_i/\mu \qquad (5)$$

$$\psi = \frac{\mu\sum_{i=1}^{N}\{K_i^T[P*o(Fj_i + \frac{1}{\mu}\gamma_i)]\} + \eta FG^T(\omega + \frac{1}{\eta}w)}{\mu\sum_{i=1}^{N}(K_i^T|P|^2 + \eta|H|^2)} \qquad (6)$$

$$\omega = \text{sgn}(GF^{-1}\psi - \frac{1}{\eta}w) \cdot \max\left(\left|GF^{-1}\psi - \frac{1}{\eta}w\right| - \frac{\tau}{\eta}, 0\right) \qquad (7)$$

Once the spectrum update is completed, the image is further denoised by guided filter, and the formula defined between the output image q and the guided image g is as follows

$$q = a_l g_s + c_l, \forall_s \in \chi_l \qquad (8)$$

where a_l and c_l are the linear coefficient and bias coefficient in window χ_l, l and s are pixel indexes, g is the guide picture, and χ_l is the window. The amplitude image acquired by the last iteration is selected as the initial image, and the amplitude image by current iteration is selected as the guided image to achieve the removal of speckle noise.

With the iterative process, the super-resolution image constantly approaches the similarity with its corresponding speckle-free image. In other words, the intervention of the TVGF method minimizes the effect of speckle noise on the image.

3. Results and Discussion

To verify the imaging characteristics of R-FP with large FOV, high resolution, and high signal-to-noise ratio, the R-FP system shown in Figure 1 was set up, and the characteristics of R-FP were demonstrated experimentally, respectively. The imaging
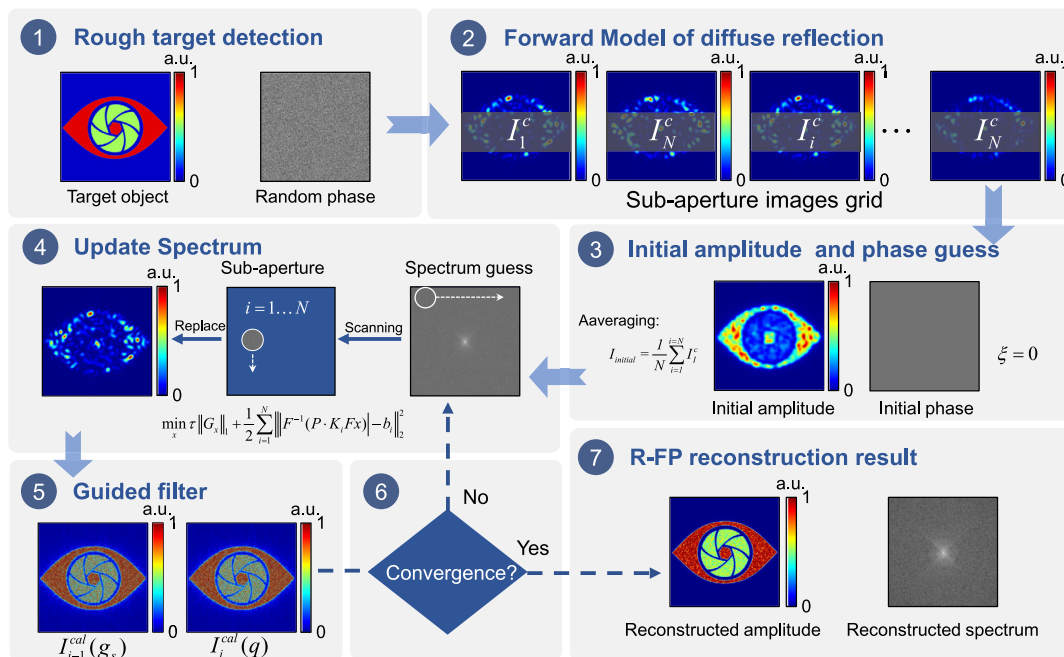

Figure 3. Flow chart of the rough target reconstructed with the proposed TVGF method.

2300180 (4 of 9)

system consists of a 75 mm FUJINON lens, a pair of 160 mm lenses to reform the Fourier domain on the aperture plane, and an 8-bit CMOS camera (DMK33UX226, Imaging Source, 4000×3000 pixels, 1.85 µm pixel size). A laser with 630 nm wavelength passed through the lens with a 75 mm focal length, forming the quasi-plane wave and illuminating the target.

3.1. Validation of R-FP to Address the FOV Attenuation Issue

We first performed long-range super-resolution imaging of spade poker with the R-FP system to validate the ability of the proposed method to enlarge the FOV of the target. The poker is placed at 1.2, 1.8, and 2.6 m from the imaging system (see Visualization 1 for the whole video recording), respectively, and fourfold resolution enhancement (11×11 subaperture images grid, recorded by 32 F-number lens) results of poker are acquired utilizing the conventional FP method and proposed R-FP method, respectively.

It is worth noting that the reconstruction results of either method would change the magnification depending on the range; for this purpose, we only focus on whether the FOV of the target would vary. **Figure 4**a is an imaging schematic diagram of the poker target utilizing the R-FP system at different imaging ranges. Figure 4b1 is the low-resolution image acquired by the FP imaging system at 1.2 m, Figure 4c1 is the corresponding high-resolution result, Figure 4d1 is the low-resolution image acquired by the R-FP imaging system at 1.2 m, and Figure 4e1 is the corresponding high-resolution result. The imaging results at 1.2 m demonstrated that the FOV of the FP result would be smaller than the FOV of the R-FP result. The distinction of FOV between FP and R-FP will be further

demonstrated in the more distant target detection, as shown in Figure 4b2–e2; the poker is placed 1.8 m away from the imaging system. Despite the variation in magnification due to the imaging range variation, the FOV of R-FP is essentially the same as in the 1.2 m case, while the FOV of FP at 1.8 m away decreases rapidly. In Figure 4b3–e3, the poker is placed 2.6 m away to simulate a further far-field imaging scenario, and the FOV of the R-FP remains the same at 1.2 and 1.8 m due to the characteristics of quasi-plane wave. However, the reconstructed result of FP at 2.6 m is barely able to express the information of the target anymore. The FOV enlargement performance of the R-FP demonstrates its ability to achieve wide field imaging at long range.

3.2. Resolution Enhancement of USAF Resolution Chart

To quantitatively analyze the effectiveness of the proposed method, we selected the USAF resolution chart with a size of $15 \text{ mm} \times 15 \text{ mm}$ as the target. In contrast to the FOV comparison experiment with poker, we increased the imaging range to 3.6 m to achieve exact resolution improvement of the target.

Quantitative super-resolution experiment on targets containing rough surfaces requires consideration of the effect of speckle noise on the imaging. Compared with the low-resolution image of the smooth target, the spectrum generated from the rough target is chaotic throughout the entire Fourier domain. The influence of speckle noise on imaging quality is quantitatively evaluated utilizing USAF resolution chart. The rough USAF spatial resolution suffering from speckle noise is 1.26 line pairs per millimeter (lp mm^{-1}) while the smooth one is 1.78 lp mm^{-1}, as shown in **Figure 5**a. With the R-FP system recording the scattering information of the target, which is demonstrated in
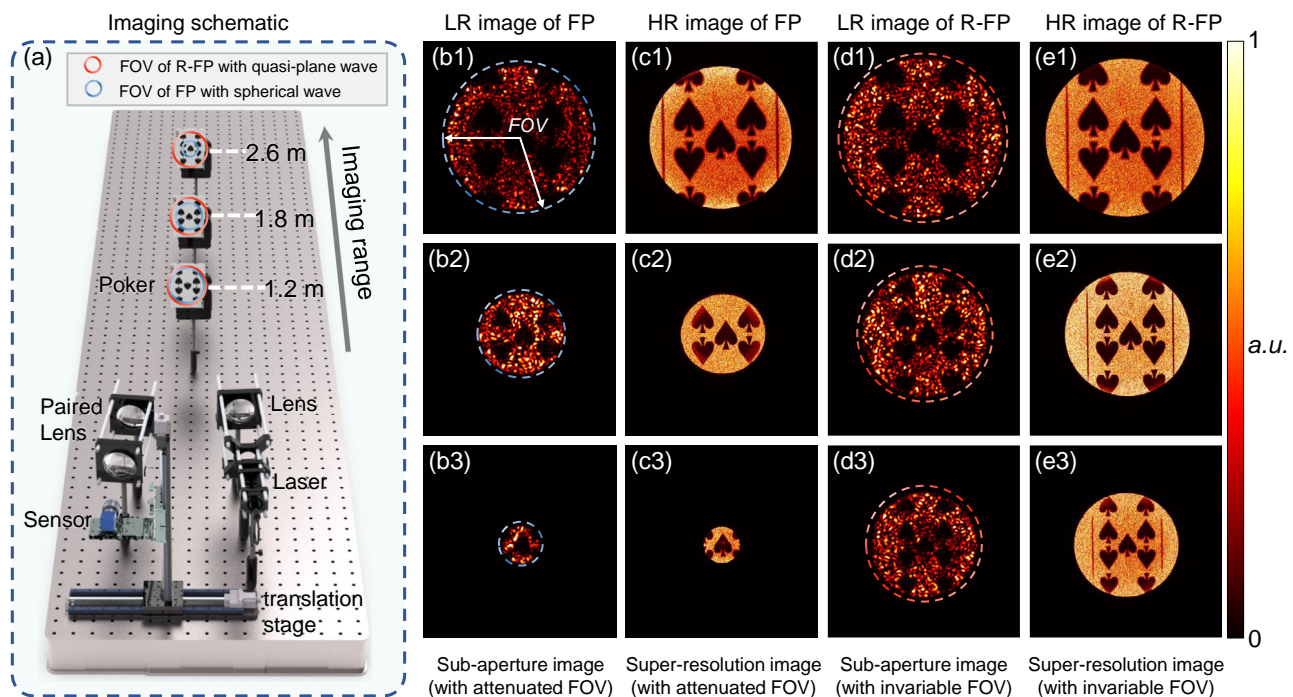

Figure 4. a) Imaging schematic of spade poker with R-FP. b,d) Low-resolution (LR) images with conventional FP and R-FP at 1.2, 1.8, and 2.6 m. c–e) High-resolution (HR) images with conventional FP and R-FP at 1.2, 1.8, and 2.6 m.
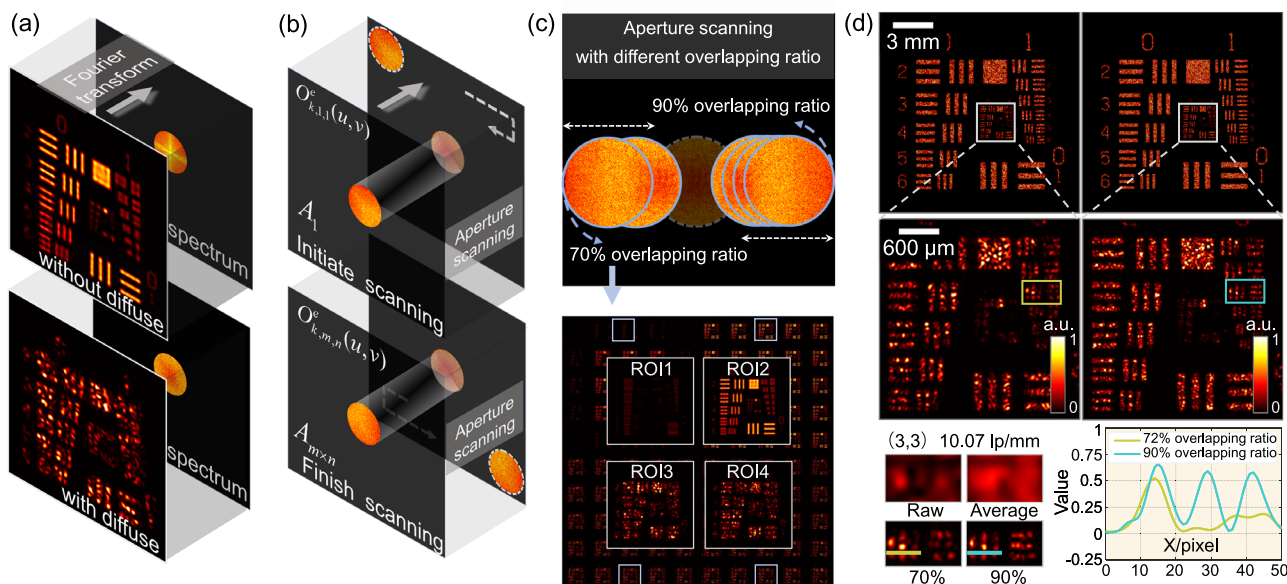
Figure 5. a) Subaperture imaging result of the smooth USAF target and rough USAF target. b) Process of the aperture scanning by the R-FP imaging system. c) Acquiring raw images by 70% overlapping ratio and 90% overlapping ratio, and the corresponding partial grids. d) Reconstructed results of the rough USAF target (70% overlapping ratio and 90% overlapping ratio), the zoom area of group 3 element 3, and the corresponding line profile.

Figure 5b, we acquired a low-resolution image grid with aperture scanning. Figure 5c illustrates the process of acquiring raw images by different overlapping ratios to verify the relationship of a higher overlapping ratio with reconstructed quality enhancement. The spacing of the aperture is essential for reconstructing high-resolution images, as it determines the overlapping ratio between subapertures during spectrum information acquisition. The effect of overlapping ratio on the reconstruction of binary and grayscale images is available in Figure S1, Supporting Information. A grid of 27×27 images (70% overlapping ratio) with 0.7 mm aperture spacing between adjacent positions was recorded, resulting in a SA with an 18.4 mm diameter. For the equivalent size of SA, a grid of 71×71 images (90% overlapping ratio) with 0.24 mm aperture spacing between adjacent positions was recorded to reduce the speckle effect of rough USAF target. The partial grids (5×5) of smooth USAF and rough USAF are shown at the bottom of Figure 5c, where the left side is a raw image with a 70% overlapping ratio and the right side is a raw image with a 90% overlapping ratio. Utilizing 27×27 images grid and 71×71 images grid, we reconstructed the super-resolution images via the R-FP method, as shown at the top of Figure 5d, where the reconstructed result with a 70% overlapping ratio is on the left side, and the result with 90% overlapping ratio is on the right side. In contrast to the raw image and cumulative averaged result, the spatial resolution of R-FP reconstructed results improved from 1.26 to 10.08 lp mm^{-1} (group 0 element 3 to group 3 element 3), which demonstrates an eightfold improvement in spatial resolution, as shown in the bottom left of Figure 5d. The corresponding line profile across the group 3 element 3 is shown at the bottom right of Figure 5d, which demonstrates the reconstructed result with data captured at a 90% overlapping ratio is improved than the ones captured at a 70% overlapping ratio.

3.3. High Signal-To-Noise Ratio Imaging of Diffuse Complex Targets with TVGF Method

The TVGF method was performed on the fingerprint specimen to demonstrate its noise immunity when the height undulation distribution is in the worst case (the related analysis of speckle noise is available in Figure S2, Supporting Information.

One of the potential application scenarios of R-FP is the long-range representation of target features, including on-the-fly authentication and on-site investigation, which requires more than simply high-resolution imaging. For instance, high-resolution imaging of fingerprint images containing speckle noise in a noncontact situation requires image denoising to achieve a detailed recording of the target features. We recorded the fingerprint image dataset by the finger on a coverslip, which consists of 29×29 (72% overlapping ratio) low-resolution images with the same system setup as the USAF experiment. The raw image and the reconstructed high-resolution result of the R-FP approach (with TVGF method) were spliced together to compare their imaging performance, as shown in **Figure 6**a. Figure 6b1–d1 illustrates diffraction blur and speckle noise of raw images in ROI1, ROI2, and ROI3. In Figure 6b2–d2, the reconstructed results with the R-FP method in ROI1, ROI2, and ROI3 present that the speckle noise still severely affects the image quality despite its improved resolution. Results with speckle noise are unacceptable in high-resolution reconstruction because in applications such as noncontact investigations, the speckle noise may still influence the judgment of the personnel involved. Figure 6b3–d3 presents the reconstructed results utilizing the R-FP method with TVGF method in ROI1, ROI2, and ROI3. In these regions, it is noticed that the resolution and image quality are improved and the speckle noise diffused in some regions is eliminated compared to those of the R-FP method without TVGF method. Furthermore, we perform the line profile
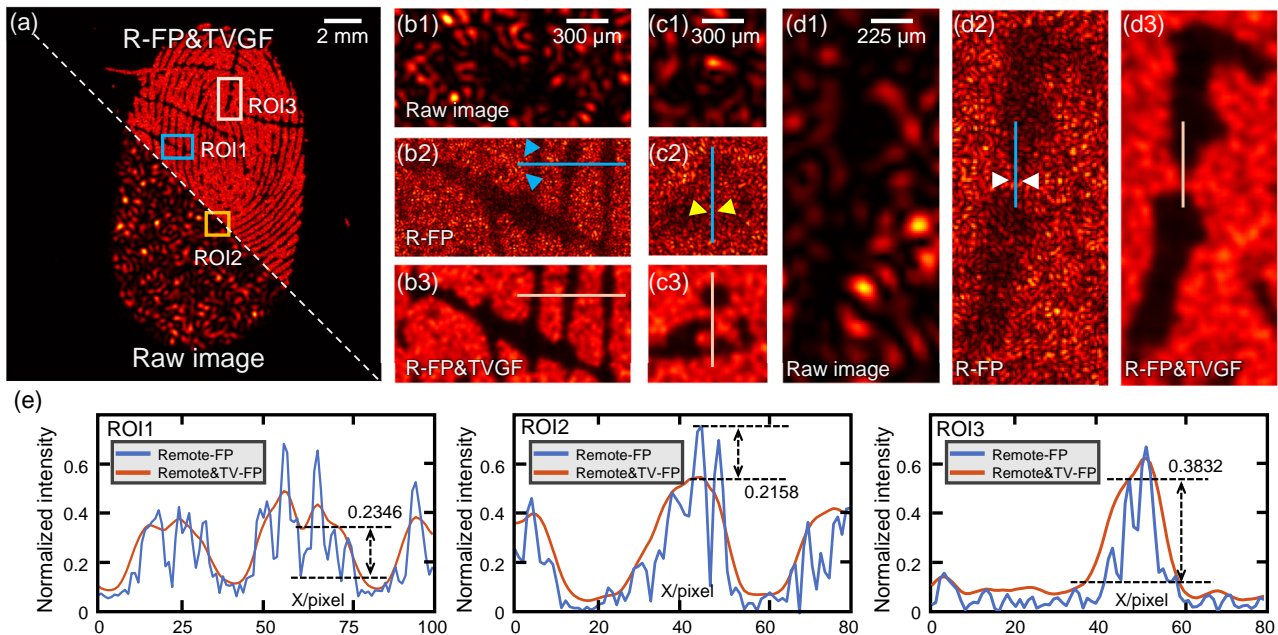
**ADVANCED
SCIENCE NEWS**

www.advancedsciencenews.com

**ADVANCED
PHOTONICS
RESEARCH**
Open Access

www.adpr-journal.com

Figure 6. a) The raw image result and the R-FP result with TVGF method. b–d) Zoom comparison of the corresponding region of interest. e) The normalized intensity distribution of the line profile in ROI1, ROI2, and ROI3.

along the blue line (R-FP method) and the red line (R-FP method with TVGF method), as indicated in Figure 6e. With TVGF, the normalized intensity of the background noise in ROI1, ROI2, and ROI3 is reduced by 0.2346, 0.2158, and 0.3832 in the maximum case, respectively. As one would expect, the robustness following the TVGF method is improved, and more texture components of the image are reproduced.

3.4. Simultaneous Wide-Field, High-Resolution, and High Signal-To-Noise Ratio Imaging at Remote Range with R-FP

Thanks to its noise immunity, wide field, and nonattenuating, the R-FP method surpasses the limits of conventional FP by detecting objects at further ranges with higher resolution. Moreover, in practical applications such as remote sensing detection, R-FP can provide characteristics of a wide field, high resolution, and high signal-to-noise ratio at the same time.

To further validate the performance of the R-FP approach, a king poker card is placed 12 m away from the imaging system to achieve the wide-field, super-resolution, and signal-to-noise ratio result with the R-FP method. The experimental setup is illustrated in **Figure 7**a. Unlike fingerprint and USAF resolution chart, the size of the poker is capable of reflecting the large FOV of R-FP, and the detailed parts of the king poker card such as the portrait and the hair are able to demonstrate the R-FP's high resolution and high signal-to-noise ratio. Figure 7b shows the poker scenario at 12 m away, and the poker was anchored to a transparent board to minimize the effect of background light on the image. In the imaging process, the detector recorded the low-resolution images by aperture scanning (32F-number with 2.3 mm aperture size), as shown in Figure 7c, and a total of 841 low-resolution images were recorded to achieve a SA of

18.4 mm. Thanks to the R-FP's utilization of quasi-plane waves to illuminate the target, most of the information on the king poker is able to record in the FOV. In Figure 7d, one of the low-resolution images is demonstrated with diffraction blur and speckle noise, which leads to indistinguishable features in the poker target. With the data from multiple angles, the cumulative averaging method is capable of suppressing the speckle noise, as shown in Figure 7e. However, it can only increase the resolution by a factor of 2 without texture information reproduction. The reconstructed result of the proposed method is presented in Figure 7f, and the resolution of the R-FP result has been further improved compared to that of the cumulative averaging method, which is more evident in the hair region of the poker card. To visualize the reconstruction results, the corresponding line profile of intensity is on the right side of the hair result. We got texture hair information by the corresponding intensity peaks in the plot, while the central intensity peak is aggravated by random speckle noise, which is more evident in the raw image. It is indicated that the proposed R-FP method can be applied to obtain texture information in areas heavily affected by speckle noise. Compared with the conventional FP approach, the reconstructed result at a range of 12 m demonstrate R-FP's advantages of wide field, high resolution, and high signal-to-noise ratio in far-field imaging.

4. Conclusion

In summary, we have developed a macroscopic FP approach based on the quasi-plane wave. By switching from spherical to quasi-plane waves for detecting targets in FP and reforming the spectrum at the imaging lens, the imaging range and corresponding FOV can be enhanced, leading to wide-field and high-resolution SA
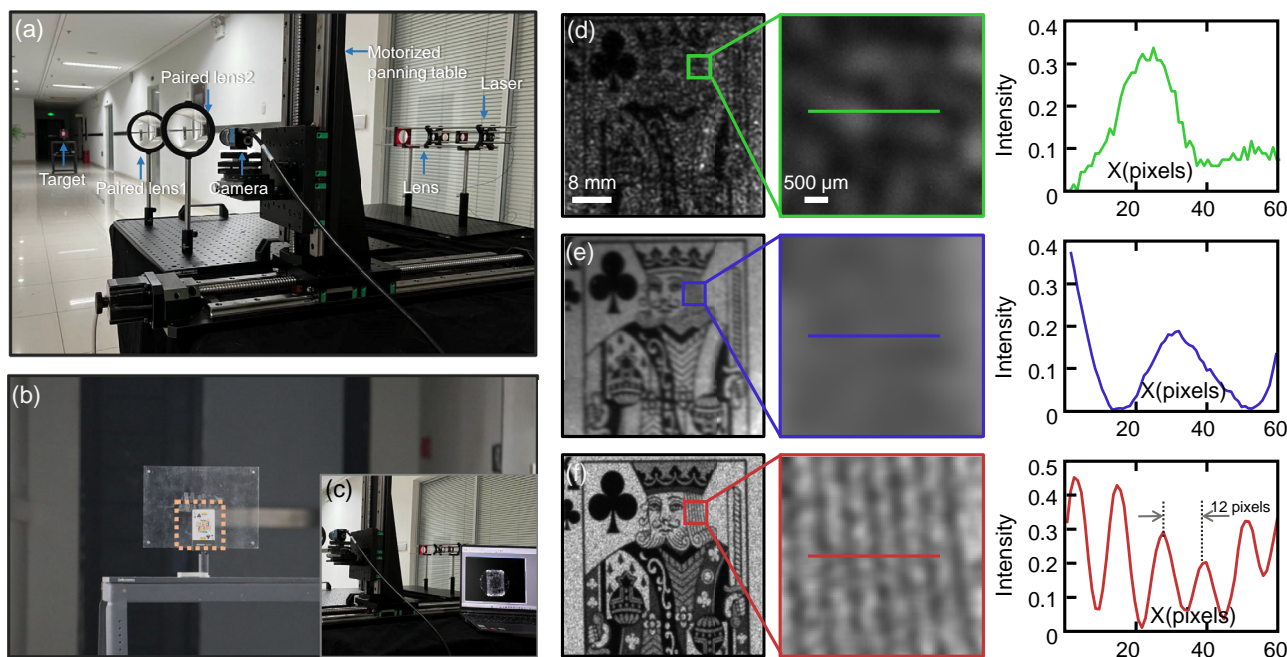
Figure 7. a) Experimental setup of the R-FP system. b) The poker card scenario as the detection target. c) Partial area enlargement of the R-FP system and low-resolution image capture. d) Raw image of target by the subaperture and corresponding line profile. e) The result of cumulative averaging method and corresponding line profile. f) Reconstruction result of R-FP with TVGF method and corresponding line profile.

detection simply and efficiently. Compared with the state-of-the-art macroscopic FP method, R-FP has demonstrated superior performance in terms of imaging FOV and imaging range, also further improving the resolution and signal-to-noise ratio of the far-field SA. Based on R-FP, we implemented SA reconstruction in a complex far-field scenario (12 m). Experimental results suggest that the R-FP approach holds the potential to achieve super-resolution imaging for remote sensing and offers a catalyst for advancing SA techniques.

Despite the promising R-FP approach, substantial challenges in the process of full-scale R-FP. High-resolution detection of moving targets continues to pose a challenge, as it requires fast imaging speeds to achieve target recording. Single-exposure imaging with camera arrays promises to achieve real-time high-resolution imaging of moving targets in space. However, the lack of overlapping ratio of camera arrays will inevitably introduce the underdetermined inverse problems, so the resolution enhancement of the image is undoubtedly diminished. Furthermore, we have been looking for the theoretical groundwork that would clearly explain the mechanisms and ways to the optimal selection of phase recovery for a complex scenario, or to profoundly comprehend why a particular denoising method is effective in a gray-scale target or not. These are among the most critical issues that will continue to attract the interest of macroscopic FP research in the SA detection community in the years to come.

Supporting Information

Supporting Information is available from the Wiley Online Library or from the author.

Conflict of Interest

The authors declare no conflict of interest.

Data Availability Statement

The data that support the findings of this study are available from the corresponding author upon reasonable request.

**ADVANCED
SCIENCE NEWS**

www.advancedsciencenews.com

**ADVANCED
PHOTONICS
RESEARCH**
Open Access

www.adpr-journal.com

[1] N. J. Miller, M. P. Dierking, B. D. Duncan, *Appl. Opt.* **2007**, *46*, 5933.

[2] J. Tang, J. Wu, K. Wang, Z. Ren, X. Wu, L. Hu, J. Di, G. Liu, J. Zhao, *Opt. Lasers Eng.* **2021**, *146*, 106707.

[3] A. Moreira, P. Prats-Iraola, M. Younis, G. Krieger, I. Hajnsek, K. P. Papathanassiou, *IEEE Geosci. Remote Sens. Mag.* **2013**, *1*, 6.

[4] M. Ryle, A. Hewish, *Mon. Not. R. Astronom. Soc.* **1960**, *120*, 220.

[5] V. Chen, M. Martorella, *SciTech Publ.* **2014**, *55* 56.

[6] M. P. Hayes, P. T. Gough, *IEEE J. Ocean. Eng.* **2009**, *34*, 207.

[7] C. Zheng, D. Jin, Y. He, H. Lin, J. Hu, Z. Yaqoob, P. T. So, R. Zhou, *Adv. Photonics* **2020**, *2*, 065002.

[8] G. Zheng, R. Horstmeyer, C. Yang, *Nat. Photonics* **2013**, *7*, 739.

[9] G. Zheng, C. Shen, S. Jiang, P. Song, C. Yang, *Nat. Rev. Phys.* **2021**, *3*, 207.

[10] P. C. Konda, P. C. Konda, L. Loetgering, L. Loetgering, L. Loetgering, K. C. Zhou, K. C. Zhou, S. Xu, A. R. Harvey, R. Horstmeyer, *Opt. Express* **2020**, *28*, 9603.

[11] Y. Fan, J. Sun, Y. Shu, Z. Zhang, G. Zheng, W. Chen, J. Zhang, K. Gui, K. Wang, Q. Chen, et al., *Laser Photon. Rev.* **2023**, *17*, 2200201.

[12] J. Sun, Q. Chen, Y. Zhang, C. Zuo, *Opt. Express* **2016**, *24*, 15765.

[13] K. Guo, Z. Zhang, S. Jiang, J. Liao, J. Zhong, Y. C. Eldar, G. Zheng, *Biomed. Opt. Express* **2018**, *9*, 260.

[14] J. Sun, C. Zuo, L. Zhang, Q. Chen, *Sci. Rep.* **2017**, *7*, 7654.

[15] H. Lee, B. H. Chon, H. K. Ahn, *Opt. Express* **2019**, *27*, 34382.

[16] C. Zuo, J. Sun, J. Li, A. Asundi, Q. Chen, *Opt. Lasers Eng.* **2020**, *128* 106003.

[17] Y. Shu, J. Sun, J. Lyu, Y. Fan, N. Zhou, R. Ye, G. Zheng, Q. Chen, C. Zuo, *PhotoniX* **2022**, *3*, 27.

[18] K. S. Park, Y. S. Bae, S.-S. Choi, M. Y. Sohn, *APL Photonics* **2022**, *7*, 096105.

[19] F. Shamshad, F. Abbas, A. Ahmed, in *ICASSP 2019-2019 IEEE Int. Conf. on Acoustics, Speech and Signal Processing (ICASSP)*, IEEE, Piscataway, NJ **2019**, pp. 7720–7724.

[20] T. Nguyen, Y. Xue, Y. Li, L. Tian, G. Nehmetallah, *Opt. Express* **2018**, *26*, 26470.

[21] Z. Zhang, T. Wang, S. Feng, Y. Yang, C. Lai, X. Li, L. Shao, X. Jiang, *Opt. Lett.* **2022**, *47*, 19.

[22] C. Zuo, J. Sun, Q. Chen, *Opt. Express* **2016**, *24*, 20724.

[23] J. Sun, Q. Chen, Y. Zhang, C. Zuo, *Biomed. Opt. Express* **2016**, *7*, 1336.

[24] S. Dong, R. Horstmeyer, R. Shiradkar, K. Guo, X. Ou, Z. Bian, H. Xin, G. Zheng, *Opt. Express* **2014**, *22*, 13586.

[25] J. Holloway, M. S. Asif, M. K. Sharma, N. Matsuda, R. Horstmeyer, O. Cossairt, A. Veeraraghavan, *IEEE Trans. Comput. Imaging* **2016**, *2*, 251.

[26] J. Holloway, Doctoral Thesis, Rice University **2016**.

[27] H. Zhang, S. Jiang, J. Liao, J. Deng, J. Liu, Y. Zhang, G. Zheng, *Opt. Express* **2019**, *27*, 7498.

[28] P. Song, S. Jiang, T. Wang, C. Guo, R. Wang, T. Zhang, G. Zheng, *Photon. Res.* **2022**, *10*, 1624.

[29] C. Wang, C. Wang, M. Hu, M. Hu, Y. Takashima, T. J. Schulz, D. J. Brady, *Opt. Express* **2022**, *30*, 2585.

[30] J. Holloway, Y. Wu, M. K. Sharma, O. Cossairt, A. Veeraraghavan, *Sci. Adv.* **2017**, *3*, e1602564.

[31] B. Cui, S. Zhang, Y. Wang, Y. Hu, Q. Hao, *Opt. Express* **2022**, *30*, 20697.

[32] J. Wu, F. Yang, L. Cao, *Opt. Lasers Eng.* **2022**, *155* 107068.

[33] B. Wang, S. Li, Q. Chen, C. Zuo, *Opt. Lett.* **2023**, *48*, 263.

[34] T. Aidukas, P. C. Konda, A. R. Harvey, M. J. Padgett, P.-A. Moreau, *Sci. Rep.* **2019**, *9*, 10445.

[35] X. Yang, P. C. Konda, S. Xu, L. Bian, R. Horstmeyer, R. Horstmeyer, R. Horstmeyer, *Photonics Res.* **2021**, *9*, 1958.

[36] J. W. Goodman, *J. Opt. Soc. Am.* **1976**, *66*, 1145.

[37] J. W. Goodman, in *Speckle Phenomena in Optics: Theory and Applications*, SPIE Press, Bellingham, WA **2020**.

[38] K. Dabov, A. Foi, V. Katkovnik, K. Egiazarian, *IEEE Trans. Image Process.* **2007**, *16*, 2080.

[39] B. Li, C. Ma, O. K. Ersoy, Z. Pan, W. Wen, Z. Sun, W. Gao, *IEEE Photonics J.* **2022**, *15*, 8500110.

[40] Z. Li, D. Wen, Z. Song, G. Liu, W. Zhang, X. Wei, *Sensors* **2018**, *18*, 3154.

[41] K. He, J. Sun, X. Tang, *IEEE Trans. Pattern Anal. Mach. Intell.* **2012**, *35*, 1397.